Material Response Modeling of MMOD Cavities

Olivia M. Schroeder*
University of Minnesota, Minneapolis, MN, 55455, United States

Prakash Shrestha†
AMA, Inc. at NASA Ames Research Center, Moffett Field, CA, 94035, United States

Grant Palmer‡
AMA, Inc. at NASA Ames Research Center, Moffett Field, CA, 94035, United States

Eric Stern§
NASA Ames Research Center, Moffett Field, CA, 94035, United States

Graham V. Candler¶
University of Minnesota, Minneapolis, MN, 55455, United States

I. Introduction

Entry, descent and landing remains a challenging and critical component of space exploration. During the entry phase, spacecraft are required to decelerate rapidly from orbital speeds to ensure safe landings. In the deceleration process, the surface of the spacecraft experiences high heating rates requiring thermal protection systems (TPS). For planetary entry, TPS are typically pyrolyzing ablative materials, meaning that they attenuate heating through mass loss and pyrolysis of infused phenolic resins.

The Mars Sample Return (MSR) Earth Entry Vehicle (EEV) [1] poses new challenges to the EDL community because of the aggressive entry conditions compounded by stringent mission reliability requirements emergent from planetary protection concerns [2]. This means it is critical that the uncertainty bounds on risk assessment be small so that the reliability requirements may be met. For nominal entries, the heat shield sizing can be done with well characterized uncertainty bounds on parameters such as the bondline temperature limit. However, for off-nominal scenarios such as a damaged heatshield, system performance is poorly characterized and modeling becomes increasingly challenging. One such scenario, with non-negligible probability of occurrence, is that the heatshield carries damage in the form of a small cavity resultant from an impact with a micro-meteoroid or orbital debris (MMOD) [3] during orbiting or interplanetary travel phase.

Some analysis can be found in the literature on modeling heating augmentation effects of hypersonic flow over cavities [4]. These modeling efforts replicated an extensive experimental campaign [5, 6] to understand the effect of different cavity geometries on the heating augmentation as part of investigations into the causes of the Columbia accident. In more recent work, arc-jet testing has been used to analyze cavity growth in ablating material samples [7].

Modeling the material response of such an environment requires the capability to capture multi-physical interactions because of the highly coupled nature of the configuration. More specifically, it is known that carbon ablation rates are directly related to heating rates. This means that heating augmentation due to a roughness element (a cavity) directly influences ablation patterns, which in turn affects flow features. Therefore, it is important to be able to capture the non-trivial shape-change in both the fluid and solid computational spaces. Material response of a cavity presents additional complexities such as heating contributions from enclosure radiation, pyrolysis gas flow near the cavity region due to surface pressure distribution effects on internal pressure gradients, and changes to heat conduction path due to material anisotropy near the cavity. Flow through the porous cavity walls and mechanical material failure are additional considerations.

In this paper, an arc-jet test campaign is used as a baseline to computationally model the flow and material response of cavities. A parametric study is designed around the baseline to study geometric effects on parameters of interest. The

*Graduate Research Assistant, AIAA Member
†Research Scientist, AIAA Member
‡Research Scientist, AIAA Member
§Research Scientist, AIAA Member
¶Professor, AIAA Fellow

US3D flow solver is used to simulate the arc-jet flow in the Aerodynamic Heating Facility (AHF) at NASA Ames [8] and generate the heating environment over material samples with cavities. The Icarus material response code is then used to simulate the multi-dimensional heating under the above conditions of samples of FiberForm with cavities.

II. Methodology

A. Computational Background

1. Flow Modeling

US3D [9–11], an unstructured, finite-volume flow solver is used to simulate the heating environment of the flow configuration considered herein. The modified Steger-Warming flux splitting method with a 2^{nd} order MUSCL scheme is used to compute inviscid fluxes. Time integration is done through data parallel line relaxation method. The Park two-temperature model is used with translational-rotational and vibrational-electronic energy mode grouping. Thermodynamic properties are computed using NASA Lewis data curve-fits. Transport properties are computed using Gupta collision integrals for viscosity and Self-Consistent Effective Binary Diffusion (SCEBD) Gupta-Yos collision integral data for diffusion.

2. Material Response Modeling

The Icarus [12] material response tool is used to simulate the heating of the FiberForm [13, 14] sample in the arc-jet. Icarus is a 3-dimensional, unstructured code that uses the finite-volume method to solve the total mass and energy conservation equations of a decomposing solid into pyrolysis gas. Additionally, the pyrolysis gas momentum is modeled through Darcy's Law. Since this work does not include a direct validation exercise with the experimental data, FiberForm is used as the material model for simplicity, however, the experiment will include a woven TPS in accordance with MSR-EEV design. Given that FiberForm does not contain resin infusion, decomposition and pyrolysis gas effects are neglected. The heating boundary conditions are treated through the surface energy balance which includes convective heating and re-radiation. Ablation terms are not considered in this work since the primary objective is to isolate and analyze only the thermal behavior of cavities in high enthalpy flow.

B. Modeling Configuration

1. Flow conditions

The modeling configuration, based on an experimental test campaign, consisted of facility max conditions of the AHF 18-inch nozzle. The arc current was 2000 amps with an estimated bulk enthalpy of 16.50 MJ/kg. Pure nitrogen is the gas used, with the inlet mass flow rate being 376 g/s. The use of nitrogen gas simplifies modeling by reducing catalytic effects to solely nitrogen recombination and allowing for the assumption that carbon nitridation, and therefore ablation, is negligible. A cold-wall, fully catalytic, boundary condition is used for the sample wall set at $T = T = 300$K. A schematic of the facility nozzle and test article modeled is shown in Fig. 1. Once the flow simulation reaches steady-state convergence, the computed face-centered wall quantities are processed to build 3-dimensional boundary conditions for the material response simulations.

2. Geometric configurations

A cavity of 36 mm diameter and 7.56 mm depth, placed along the centerline, $INSERT$ mm distance from the stagnation point is used as a baseline configuration for a parametric study. The solid domain consists of a rectangular block of length 100mm, height of 14.5mm and 56.5 mm width. placed at a 20 deg angle. The diameter of the baseline configuration will be referred to as D_0 and the depth h_0. The simulations were run using a single material block of FiberForm. The heating boundary condition parameters are applied to the solid grid boundary faces through a nearest-neighbor search. The parametric study is constructed around this baseline configuration in two ways: 1) Varying depth: $0.5h_0$, h_0, $1.5h_0$; 2) Varying shape by modifying the diameter of the cavity floor: $0.75D_0$ (convergent), D_0 (cylindrical), $1.25D_0$ (divergent). Here D_0 is the diameter of the top of the cavity. A diagram of all configurations simulated is shown in Fig. 2. It is worth noting that each of these cavity configurations correspond to a different fluid dynamics and material response computational grids.

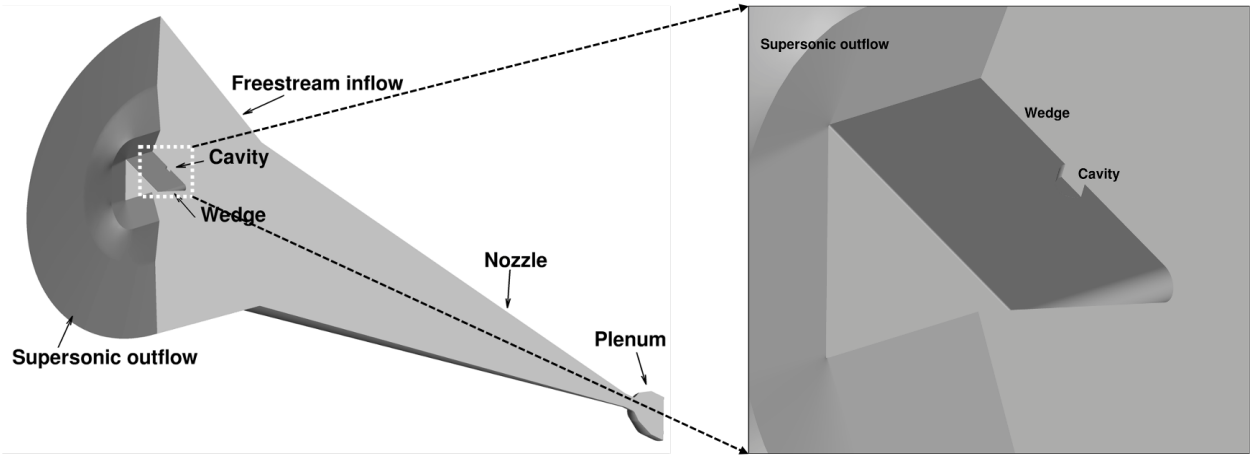

Fig. 1 Schematic of computational configuration.

3. Computational Grids

Since the test article considered is a wedge, the geometry is symmetric and therefore it is only necessary to simulate half of the domain. The computational mesh for the fluid domain is shown in Fig. 2. Hexahedral elements are used in the nozzle region as well as the post-shock region near the article surface, for accurate heat flux capturing. A layer of tetrahedral elements is added in the flow expansion region ahead of nozzle and away from the boundaries. The 3-dimensional mesh for the solid domain is shown in Fig. 3. It is composed of $\backsim 300,000$ hexahedral elements. A grid convergence study performed on a $\backsim 600,000$ element grid showed no significant difference in temperature at specific sampling locations.

III. Results

A. Baseline Solution

The solution for the baseline cavity configuration is shown in Fig. 4. The Mach number contours of the flow through the nozzle is shown is shown in Fig. **??** and the flow over the sample as well as the resulting wall heat flux are shown in Fig. 4b. Finally, the material response solution to the flow environments simulated is shown in Fig. 4c. One can observe that the region upstream of the cavity is hottest purely due to the wedge geometry. However, one can also note a peak in the surface temperature at the impingement point of the fluid. It is apparent that the cavity floor is significantly cooler than the surface of the wedge, despite a relatively hotter circular region near the cavity wall.

B. Multi-Dimensionality

In many TPS design applications, 1-dimensional analysis can provide rapid solution turn-over and is an allowable approximation within a known tolerance to the multi-dimensional problem. In cavity heating however, the heat flux to the surface is not uniform and this drives multi-directional temperature gradients in the material. Additionally, the current configuration features an anisotropic material (thermal conductivity is not equivalent in the in-plane and transverse fiber directions) at a 70 deg angle relative to the flow (from the wedge).

Therefore, it is of interest to quantify what how multi-dimensional the configuration is in the resulting in-depth temperatures at various locations along the sample. To this effect, the model was simulated in 1- and 2-dimensions where the 1-dimensional cases consisted of three simulations at each thermocouple station. The 2-dimensional case consisted of a one cell extrusion of the symmetry plane of the 3-dimensional. The thermocouples for each station was placed at 1 mm, 2 mm, and 4 mm from the surface, and the stations were placed at a distance d upstream of the cavity, downstream of the cavity and under the center of the cavity. The in-depth temperatures were compared in time and are shown in Fig. 5. It can be noted from Fig. 5 that the temperature in regions far enough upstream of the cavity does not become significantly affected and a 1-dimensional approximation could be acceptable. However, directly

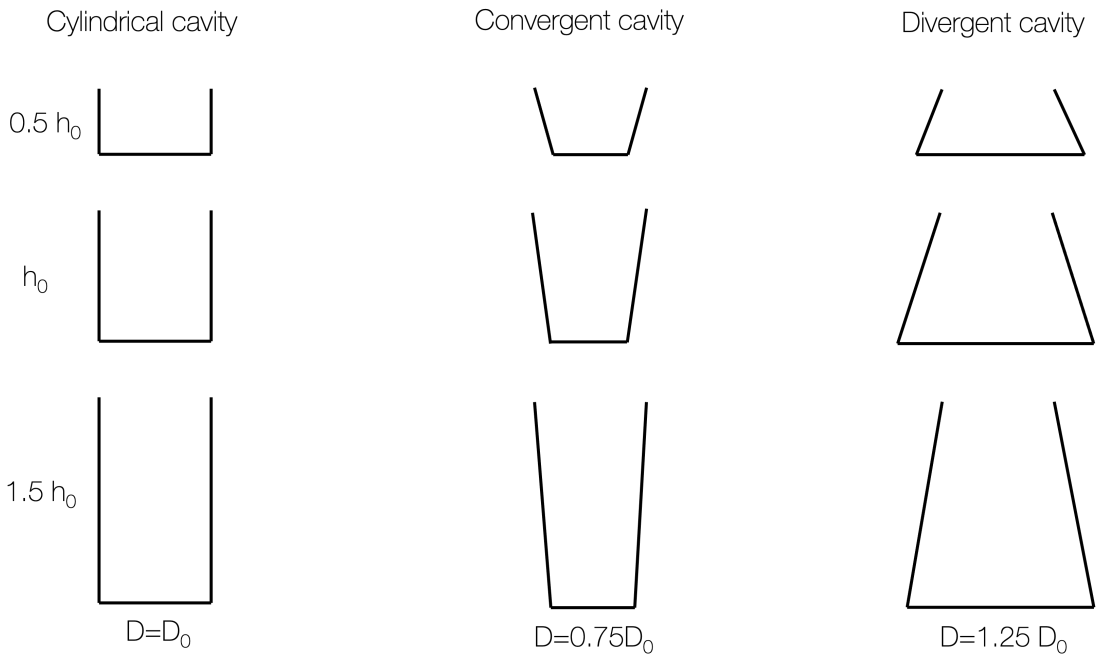

Fig. 2 Parametric study configurations.

under the cavity, the 1-dimensional approximation diverges from the 2-dimensional solution significantly suggesting that the gradients generated at the surface from the heating profile constitute a non-negligible effect in modeling this configuration.

C. Parametric Study

The results to the parametric study will be presented and analyzed in the current section. The flow behavior in the various cavities is shown in Fig. 6 and will be used to explain some of the findings of this study. First, we note that in all cavities, there is a re-circulation region inside the cavity induced by the shear of fast moving flow over the top of the cavity, however, note that the velocity associated with the re-circulation bubbles is relatively low compared to the boundary layer on the sample surface and therefore, the contribution to the heating of this re-circulation is relatively small. Secondly, in all cavities it is apparent that for these flow conditions, the diameter is large enough to allow flow to enter the cavities before impinging on the wall. One observation that can be made regarding this point is that the depth that the flow reaches is more dependent on the shape of the cavity than the depth. The divergent shape allows for the most flow to enter the cavity and the convergent shape allows for the least, with the cylindrical shape being in between. The remaining section will focus on the material response to these flow configurations, and the analysis will focus on:

1) Effect of cavity depth (where shape is held constant)
2) Effect of cavity shape (where depth is held constant).

1. Effect of cavity depth

For the configuration mentioned in the previous section, the effect of varying cavity depth is investigated. The cavity diameter is kept constant, and three cavity depths are simulated: a baseline (h_0, a shallow cavity $0.5h_0$, a deeper cavity $1.5h_0$. The resulting surface and bondline temperature along the symmetry plane of sample is shown in Fig. 7.

Figure 7a presents the surface temperature along the symmetry line of the sample. One can observe that the temperature along the surface of the wedge with no cavity present slightly decreases along the distance. With the introduction of the cavities, one can see that regardless of their depths, the temperature drops significantly once the cavity is reached, at approximately 2 cm. Inside the cavity, from 2 cm to 3.5 cm, the temperature increases until approximately 3.1 cm before decreasing again until the back-wall of the cavity is reached. Once the wall is reached, the flow impingement causes a spike followed by a sharp decrease in temperature until the nominal state is again reached,

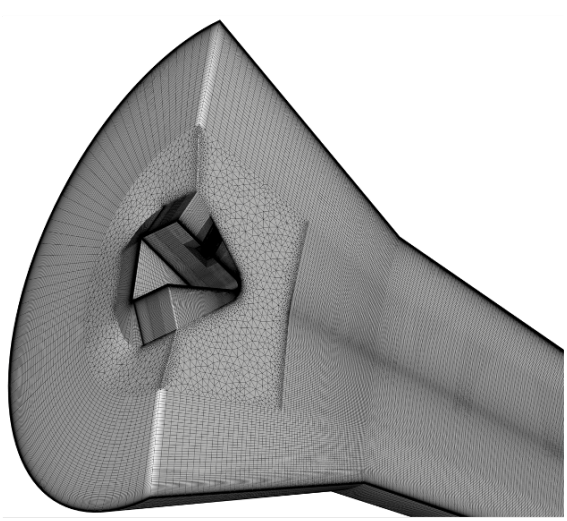

(a) 3-dimensional view of flow expansion region.

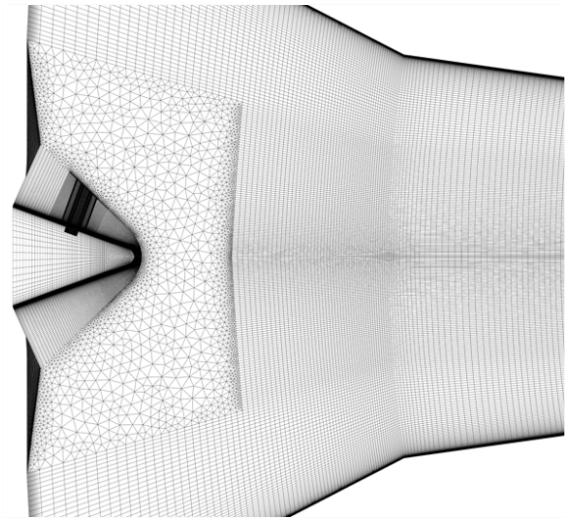

(b) Planar view of nozzle exit region.

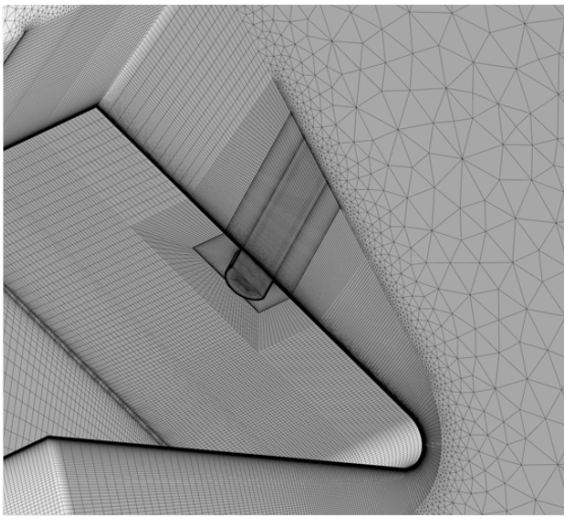

(c) Post-shock region and sample wall topology.

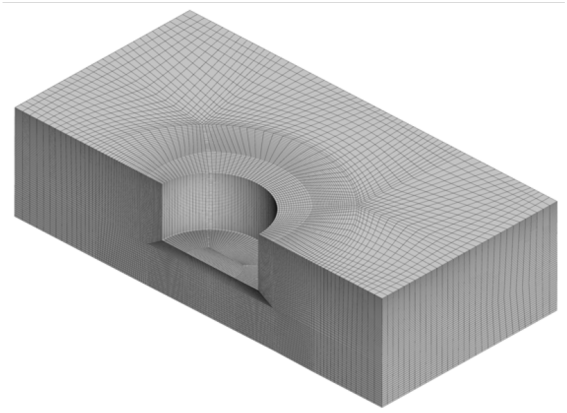

(d) Post-shock region and sample wall topology.

Fig. 3 Computational grid for solid domain for the baseline cavity.

around 4.5 cm. The shallowest cavity observes the highest surface temperature, followed by the mid-depth, and finally the deepest cavity observes the lowest surface temperature. This can be explained from the fact that the shallow cavities have a smaller volume of cold fluid and that the distance between the high enthalpy flow in the boundary layer to the bottom of the cavity is reduced, thus increasing the heating to the surface; analyzing Fig 6 columnwise (increasing depth) highlights this fact.

Figure 7b show the temperature at the bondline of the sample along the symmetry plane. For a case with no cavity, the temperature steadily decreases over the distance. The deepest cavity observes the highest increase in temperature relative to the nominal case, where the maximum reaches almost 875 K at approximately 3cm, an augmentation of approximately 1.6 of the baseline bondline temperature. The mid-depth case, also observes an increase in temperature following approximately a shape of a bell-curve where the maximum is approximately 640 K, or 1.2 factor augmentation. Finally, the shallow cavity behaves differently in that the temperature actually decreases to approximately 500 K at near entrance of the cavity, around 2 cm, and then increases to reach a maximum of 530 K, or 1.04 augmentation, around 3.5 cm. The difference in behavior between the shallow cavity and the mid- and deep cavity is due to competing mechanisms. In the mid- and deep cases, the dominating factor affecting the bondline temperature is the loss of thermal mass in the cavity and the reduction of the conduction path from the surface of the cavity to the bondline. This means

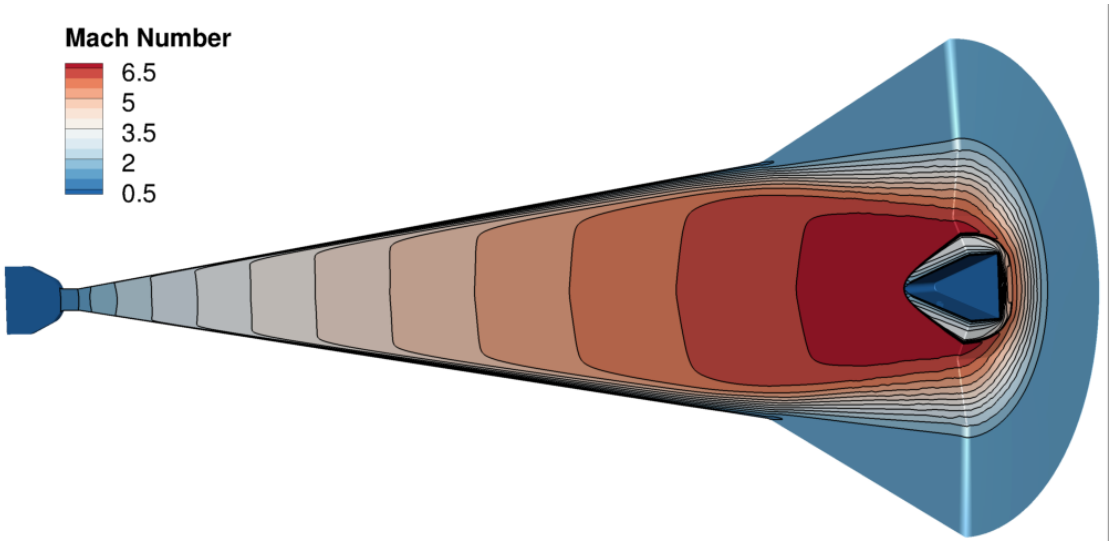

(a) Flow through AHF nozzle.

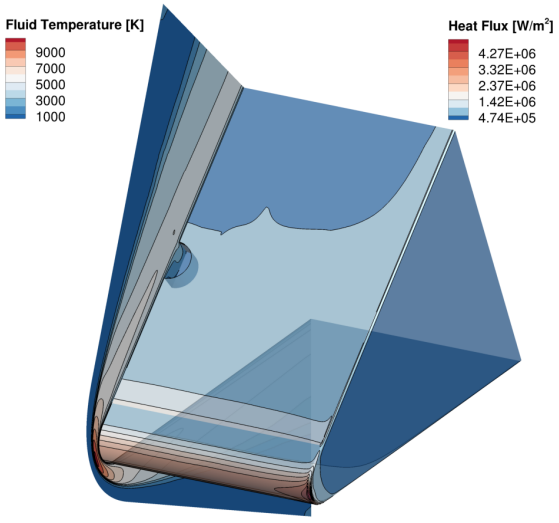

(b) Flow over wedge article with baseline cavity configuration.

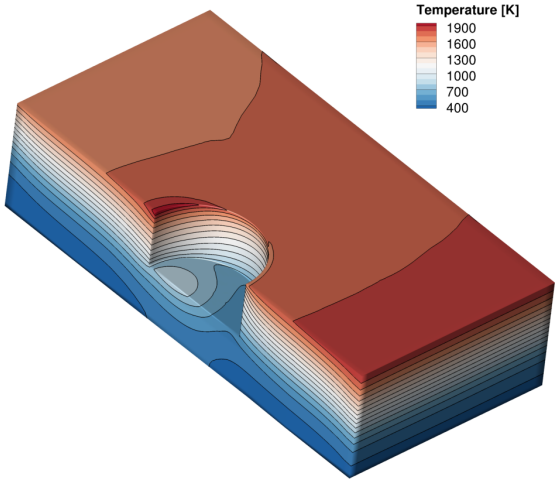

(c) Material response of FiberForm sample with baseline cavity.

Fig. 4 Baseline fluid and solid solution.

that despite the drop in surface temperature in the cavity, the reduced conduction path is enough to overcome this drop and highly increase the peak bondline temperature. In the case of the shallow cavity, the bondline temperature is mostly driven by the surface phenomena because the loss in conduction path is not significant enough to drive bondline temperature behavior. This explains why a decrease in bondline temperature is observed relative to the nominal solution in that the drop in surface temperature drives a drop in bondline temperature. The small increase in temperature at the bondline that follows, around 3.5 cm is driven by the same increase seen at the surface at the same location. In summary, it has been shown that the bondline temperature is weakly dependent on the surface state and is primarily determined by the length of the conduction path and the thermal mass (volume of mass reduction). The shorter the conduction path becomes, the more likely the bondline temperature will increase significantly even if the surface temperature is lower. It should also be noted that all cavities presented the same peak surface temperature, suggesting that the flow impingement, and subsequent heating augmentation, is not significantly affected by the depth of the cavity, as is observed in Fig. 6.

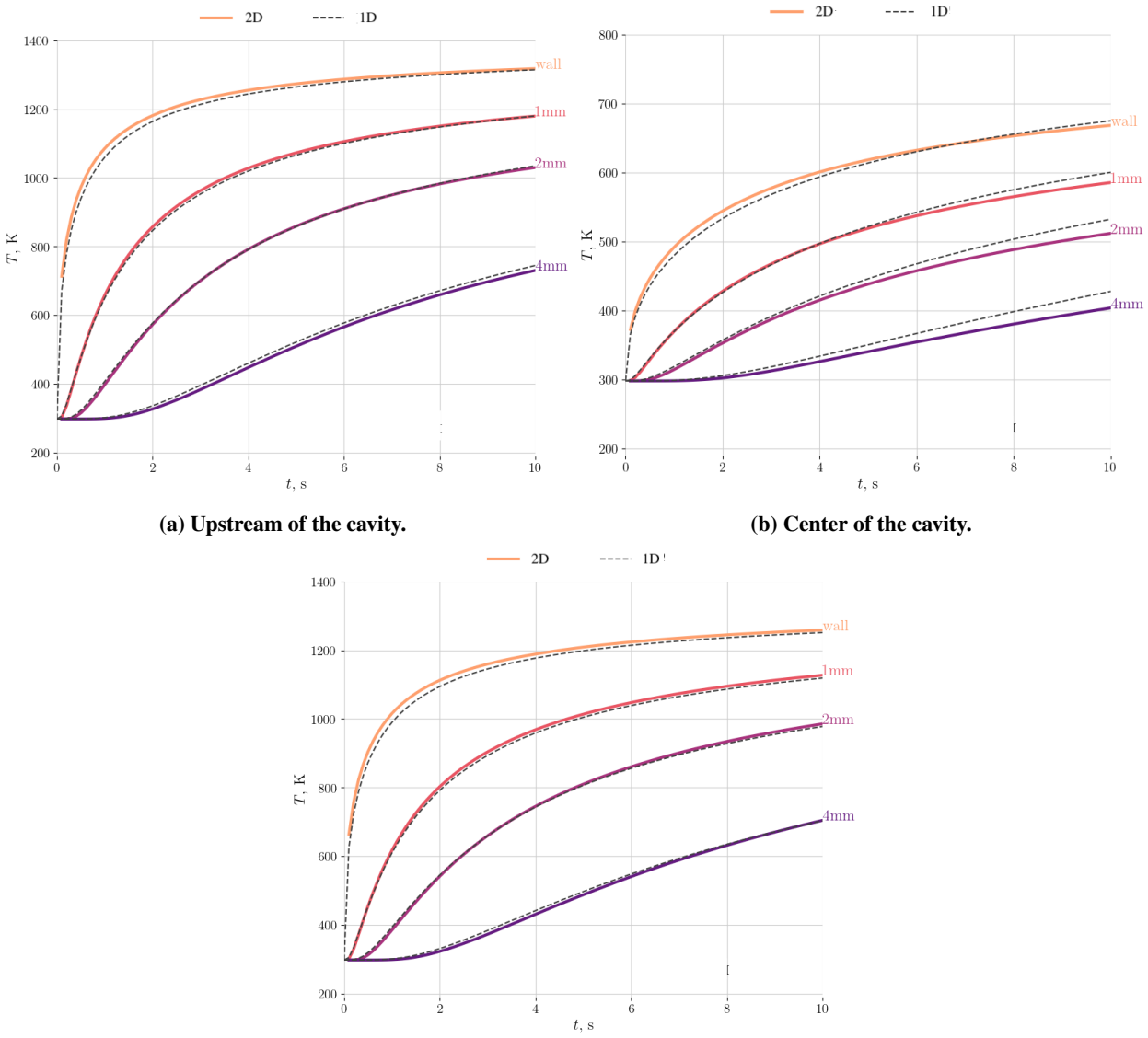

(a) Upstream of the cavity.

(b) Center of the cavity.

(c) Downstream of the cavity.

Fig. 5 In-depth temperatures in time at three locations.

2. Effect of cavity shape

The effect of varying the ratio of the top to bottom diameters of the cavities is investigated, with the purpose of highlighting the effect of shape on the resulting heating patters and ultimately the bondline temperature. The effect of shape is investigated on the three cavity depths described in the previous section in order to understand if the trends found hold for different the depths. Cavities with a ratio of top to bottom diameter of 0.75, 1.0, 1.25 were analyzed for each depth of h_0, $0.5h_0$, $1.5h_0$.

The surface temperature of the cavities is shown in Fig. 8a, and the respective bondline temperatures are shown in Fig. 8b. First, examining the shallow cavity types, one can observe that the surface temperature is highest for the convergent type both at the bottom of the cavity and at the impingement point. The mid-depth cavities appear to have very little dependence of shape on surface temperature. Finally, the deep cavities behave differently in that the divergent shape has the largest increase in surface temperature, followed by the cylindrical shape, and the lowest being the convergent shape. The distinct behavior between these cavity shapes suggests that there are competing mechanisms that dominate the heating for different depths. It is not immediately clear which mechanisms leads to each scenario, however, aspects to

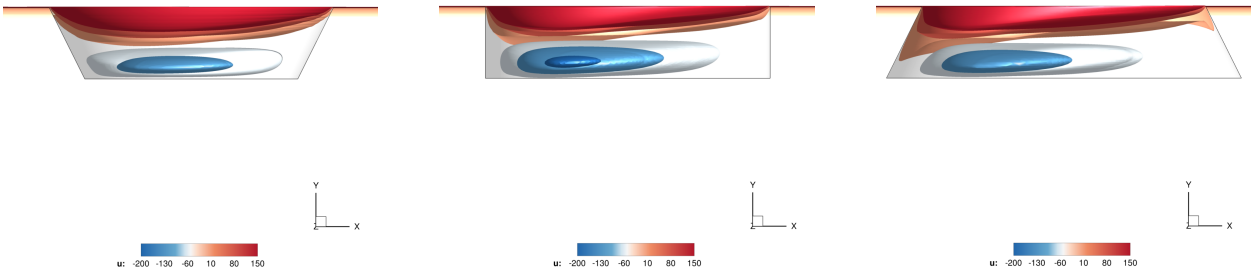

(a) $h = 0.5h_0$, $D = 0.75D_0$ **(b)** $h = 0.5h_0$, $D = D_0$ **(c)** $h = 0.5h_0$, $D = 1.25D_0$

(d) $h = h_0$, $D = 0.75D_0$ **(e)** $h = h_0$, $D = D_0$ **(f)** $h = h_0$, $D = 1.25D_0$

(g) $h = 1.5h_0$, $D = 0.75D_0$ **(h)** $h = 1.5h_0$, $D = D_0$ **(i)** $h = 1.5h_0$, $D = 1.25D_0$

Fig. 6 Flow interaction with cavities.

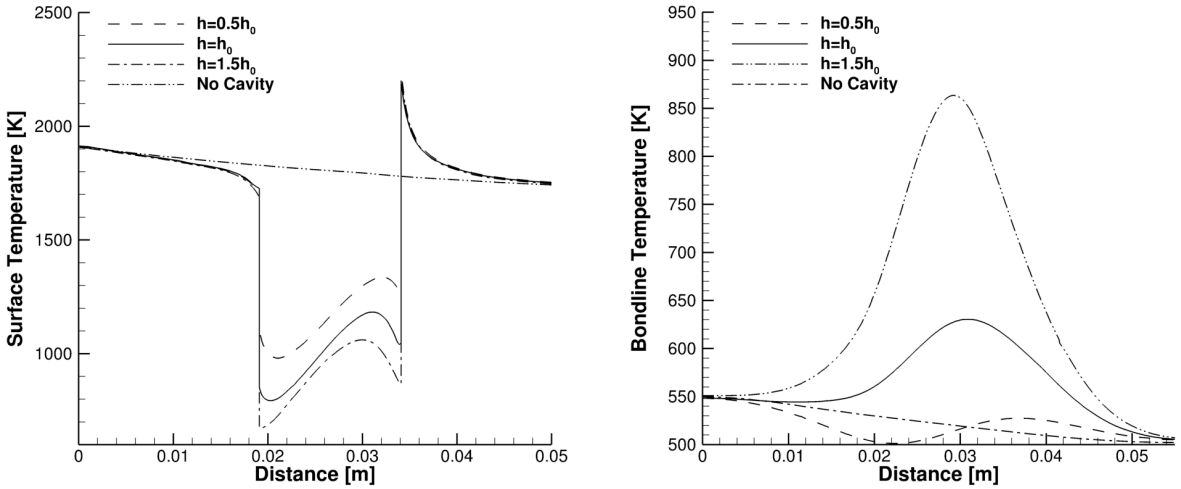

(a) Surface temperature. **(b) Bondline temperature.**

Fig. 7 Temperature for various cavity depths.

consider are:

1) Flow re-circulation;
2) Distance from the cavity floor to the high enthalpy gas;
3) Flow impingement point (affected by the angle of the cavity wall);
4) Overall cavity volume (larger volume contains more cold gas).

The bondline temperature of the shallow cavities, Fig. 9a follows the trend of the surface temperature. The convergent type cavity observes the largest increase from the baseline case, followed by the cylindrical shape, and the lowest peak is observed by the divergent shape. Additionally, the shallow cavities observe a dip in bondline temperature, which is most pronounced in the divergent case, due to the respective drop in surface temperature. The mid-depth cavities, Fig. 9b demonstrate the highest spike in bondline temperature for the divergent shape, followed by the cylindrical shape, and lowest for the convergent shape. It should be noted that for cavities of this depth, the shape effects do not appear to play a significant role in the bondline temperature being that the range of maximum temperature varies less than 50 K between all three shapes. Finally, the deepest cavities, Fig. 9c display the same trend in bondline temperature, convergent being the lowest, followed by cylindrical, and divergent being the highest. However, in contrast with the mid-depth cavities, the spread of the peaks is significant, approximately 150 K, implying that the interaction of the divergent shape and the larger depth contribute to the augmentation of the bondline temperature significantly. Physically, the trend observed in the mid-depth and deep cavities can be justified through by the fact that for the same depth, the convergent cavities have the smallest volume, followed by the cylindrical cavities, and the divergent cavities present the largest volume. It follows that the divergent cavities would then have the least thermal mass, followed by the cylindrical ones, and finally the convergent cavities would have the most. Less thermal mass implies there is less material to attenuate the heat as it is transferred to the bondline which translates into a higher temperature.

D. Summary of parametric study

In order to capture and synthesize the results presented above, Fig. 10 shows a plot of the maximum bondline temperature normalized by the bondline temperature of a sample with no cavity at the corresponding location. The trends show that as the depth of the cavities increase the effect of the cavity shape becomes amplified. This is because the loss of thermal mass becomes significant, and as the depth increases, the volume of mass lost due to the angle of the walls scales with the product of the depth with the squared power of the diameters. The trend further shows that within the parametric space analyzed, a deep cavity of divergent shape would prove to be the worst case scenario with an augmentation of the bondline temperature of approximately 1.9. Finally, the trend suggests that the cavity depth is be the primary parameter of concern with regards to bondline temperature considering that the mildest shape, convergent

cavity, at a large depth still suffer an augmentation of approximately 50% relative to a mid-depth, divergent shape.

IV. Conclusions

High enthalpy flow through the AHF 18-inch nozzle is simulated over a wedge sample with a cylindrical cavity. A 2-dimensional boundary condition was reconstructed from the CFD solution and imposed on a material response simulation of a sample of FiberForm. Analysis of heat conduction was performed in 1, and 2-dimensions and shows that the 1-dimensional analysis agrees well with 2-dimensional analysis in regions far from the cavity but that near the cavity heat conduction is inherently multi-dimensional. A parametric study was performed around a baseline cavity in which the shape was varied as well as the depth. Three shapes, convergent, cylindrical, and divergent cavities were simulated at three depths, $0.5h_0$, h_0, and $1.5h_0$. The study showed that the most significant parameter in affecting the bondline temperature was the conduction path (deeper cavities experience higher bondline temperatures), the secondary driver is volume due to loss of thermal mass. It was also found that if the cavity is shallow enough the dominant parameter is the surface heat flux although the bondline temperature augmentation in these cases is generally negligible.

V. Future Work

The analysis presented herein has assumed that no ablation takes place. This assumption, while consistent with the planned experimental campaign, does not offer insight into what types of ablation patterns result from the cavity presence, or how recessed material changes the conduction path to possibly induce failure to meet bondline temperature requirements. Exploration of shape change is planned by using the mesh motion capability of Icarus. Additionally, this analysis does not account for the coupling between the fluid and solid domains, neither in the exchange of thermal information at the boundary nor in the coupled shape change driven by gas surface interaction chemistry. Future work will include the coupling of these effects with the recently developed Ares code [15]. Finally, rigorous validation against the experimental data will provide insight into the accuracy of the current modeling approach as well as elucidate as to whether additional mechanisms not captured in the current framework need be considered.

Acknowledgments

The primary author is funded by a NASA Space Technology Graduate Research Opportunities (NSTGRO) under Grant Number 80NSSC18K1150. Support from ONR MURI Grant number N00014-20-1-2682 is also acknowledged. Additional support provided by NASA's Mars Sample Return Earth Entry Vehicle (MSR-EEV) project, and the Space Technology Mission Directorate (STMD) Entry Systems Modeling (ESM) project.

References

[1] Dillman, R., and Corliss, J., "Overview of the Mars Sample Return Earth Entry Vehicle," *6th International Planetary Probe Workshop*, Atlanta, GA, 2008.

[2] Hyde, J. L., Bjorkman, M. D., Hoffman, K. D., Christiansen, E. L., Lear, D. M., and Prior, T. G., "Micrometeoroid and Orbital Debris Threat Assessment: Mars Sample Return Earth Entry Vehicle," Technical Report 20140001399, NASA Lyndon B. Johnson Space Center, Houston, Texas, September 2011.

[3] Christiansen, E. L., Arnold, J., Davis, A., Hyde, J., Lear, D., Liou, J.-C., Lyons, F., Prior, T., Ratliff, M., Ryan, S., Giovane, F., Corsaro, B., and Studor, G., "Handbook for Designing MMOD Protection," Technical Report TM-2009-214785, NASA Johnson Space Center, Houston, Texas, June 2009.

[4] Palmer, G. E., Alter, S., Everhart, J., Wood, W., Driver, D., Brown, J., and Prabhu, R. K., "CFD Validation for Short and Long Cavity Flow Simulations," *AIAA 2007-4254*, 2007.

[5] Everhart, J. L., Alter, S. J., Merski, N. R., Wood, W. A., and Prabhu, R. K., "Pressure Gradient Effects on Hypersonic Cavity Flow Heating," *AIAA 2006-0185*, 2006.

[6] Everhart, J. L., Berger, K. T., Merski, N. R., Wood, W. A., Hollingsworth, K. E., Hyatt, A. J., and Prabhu, R. K., "Aero-Heating of Shallow Cavities in Hypersonic Freestream Flow," Tech. Rep. TM–2010-216846, NASA, 2010.

[7] Agrawal, P., Munk, M. M., and Glaab, L. A., "Arcjet Testing of Micro-Meteoroid Impacted Thermal Protection Materials," *AIAA 2013-2903*, 2013.

[8] Terrazas-Salinas, I., "Test Planning Guide for NASA Ames Research Center Arc Jet Complex and Range Complex," Tech. Rep. A029-9701-XM3 Rev. G, NASA Ames Research Center, Moffett Field, CA 94035, January 2021.

[9] Nompelis, I., Drayna, T., and Candler, G., "A Parallel Unstructured Implicit Solver for Hypersonic Reacting Flow Simulation," *AIAA 2005-4867*, 2005.

[10] Nompelis, I., Drayna, T., and Candler, G., "Development of a Hybrid Unstructured Implicit Solver for the Simulation of Reacting Flows Over Complex Geometries," *AIAA 2004-2227*, 2004.

[11] Candler, G. V., Johnson, H. B., Nompelis, I., Gidzak, V. M., Subbareddy, P. K., and Barnhardt, M., "Development of the US3D Code for Advanced Compressible and Reacting Flow Simulations," *AIAA 2015-1893*, 2015.

[12] Schulz, J. C., Stern, E., Muppidi, S., Palmer, G., Schroeder, O., and Martin, A., "Development of a three-dimensional, unstructured material response design tool," *AIAA 2017-0667*, 2017.

[13] Panerai, F., Ferguson, J. C., Lachaud, J., Martin, A., Gasch, M. J., and Mansour, N. N., "Micro-tomography based analysis of thermal conductivity, diffusivity and oxidation behavior of rigid and flexible fibrous insulators," *International Journal of Heat and Mass Transfer*, Vol. 108 Part A, 2017, pp. 801–811.

[14] Panerai, F., White, J. D., Cochell, T. J., Schroeder, O. M., Mansour, N. N., Wright, M., and Martin, A., "Experimental measurements of the permeability of fibrous carbon at high temperature," *International Journal of Heat and Mass Transfer*, Vol. 101, 2016, pp. 267–273.

[15] Schroeder, O., Brock, J., Stern, E., and Candler, G., "A coupled ablation approach using Icarus and US3D," *AIAA 2021-0924*, 2021.

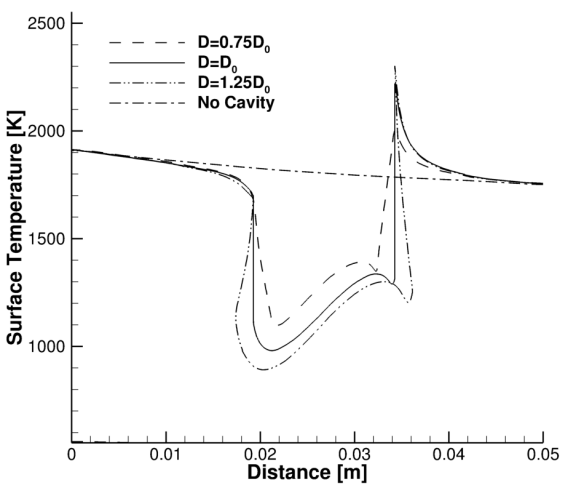

(a) Shallow cavities.

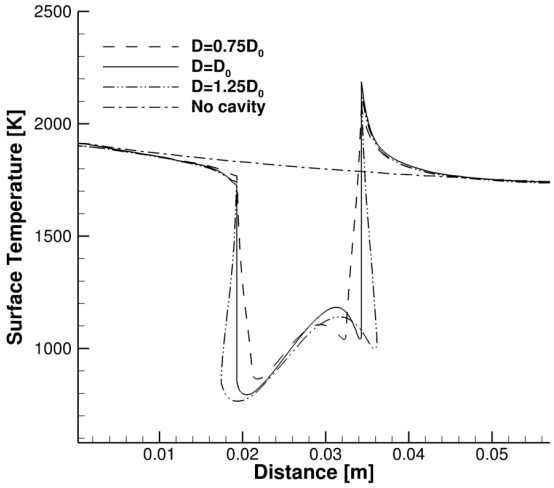

(b) Mid-depth cavities.

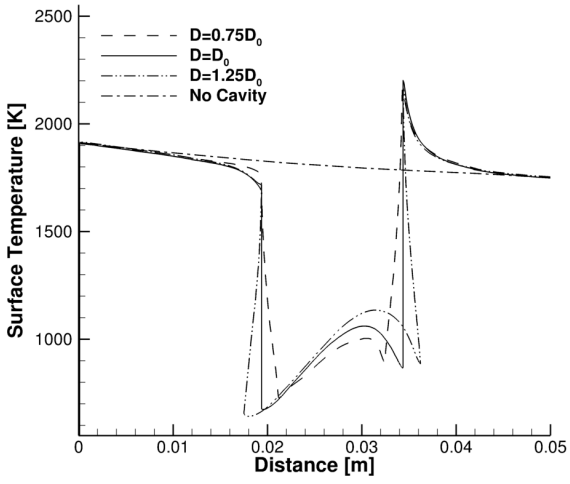

(c) Deep cavities.

Fig. 8 Surface temperature of various cavity shapes.

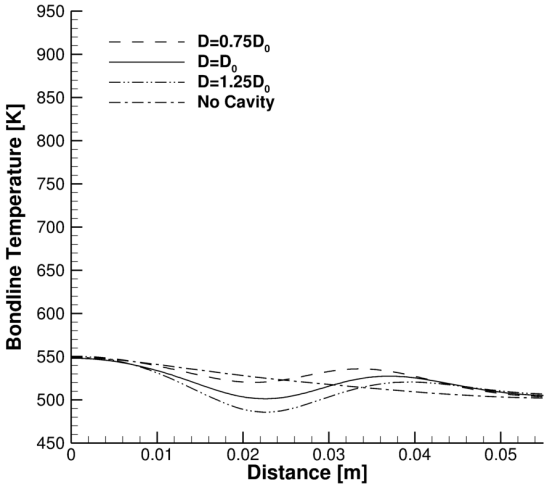

(a) Shallow cavities.

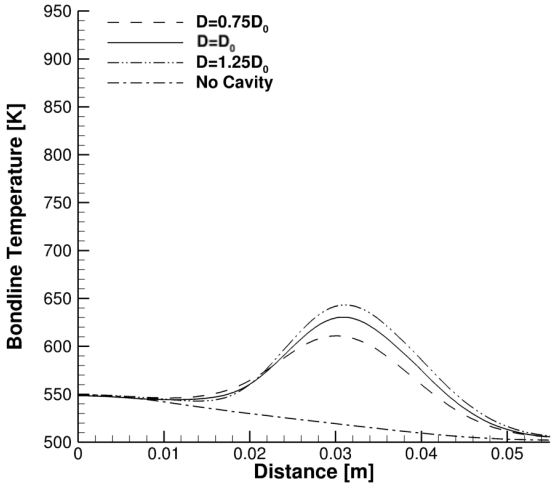

(b) Mid-depth cavities.

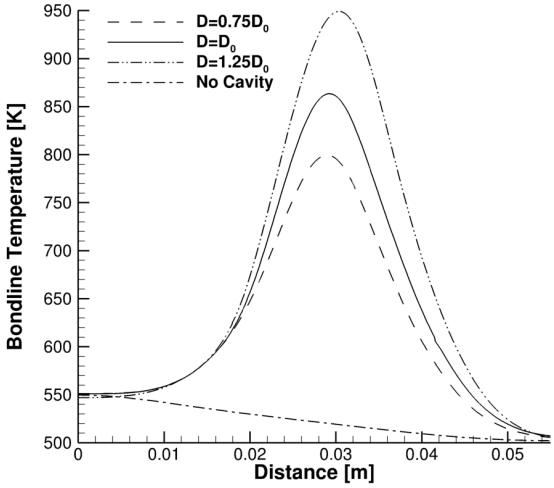

(c) Deep cavities.

Fig. 9 Bondline temperature of various cavity shapes.

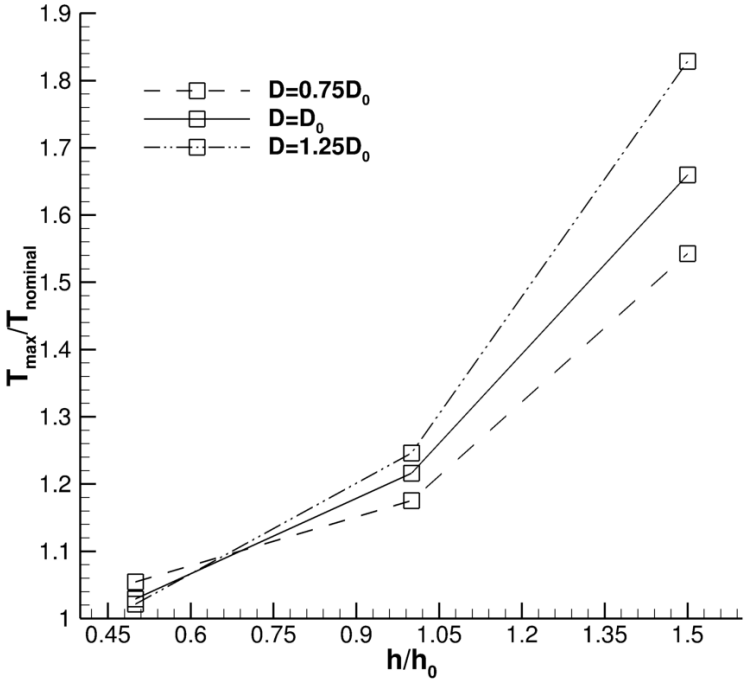

Fig. 10 Shape parameter effect on maximum bondline temperature increase.